City Research Online

City, University of London Institutional Repository

This is the unspecified version of the paper.

This version of the publication may differ from the final published version.

Aligning Scan Acquisition Circles in Optical Coherence Tomography Images of The Retinal Nerve Fibre Layer

Haogang Zhu, David P Crabb*, Patricio G Schlottmann, Gadi Wollstein, David F Garway-Heath

Abstract—**Optical coherence tomography (OCT) is widely used in the assessment of retinal nerve fibre layer thickness (RNFLT) in glaucoma. Images are typically acquired with a circular scan around the optic nerve head. Accurate registration of OCT scans is essential for measurement reproducibility and longitudinal examination. This study developed and evaluated a special image registration algorithm to align the location of the OCT scan circles to the vessel features in the retina using probabilistic modelling that was optimised by an expectation-maximization algorithm. Evaluation of the method on 18 patients undergoing large numbers of scans indicated improved data acquisition and better reproducibility of measured RNFLT when scanning circles were closely matched. The proposed method enables clinicians to consider the RNFLT measurement and its scan circle location on the retina in tandem, reducing RNFLT measurement variability and assisting detection of real change of RNFLT in the longitudinal assessment of glaucoma.**

Index Terms—**image registration, probabilistic modelling, expectation-maximization, optical coherence tomography, scan circle alignment**

H. Zhu is with the Department of Optometry and Visual Science, City University London, Northampton Square, EC1V 0HB, United Kingdom; and NIHR Biomedical Research Centre for Ophthalmology, Moorfields Eye Hospital NHS Foundation Trust and UCL Institute of Ophthalmology, 162 City Road, London, EC1V 2PD, UK (e-mail: haogangzhu@gmail.com).

D. P. Crabb is with the Department of Optometry and Visual Science, City University London, Northampton Square, EC1V 0HB, UK (phone: +44 (0) 2070400191; e-mail: d.crabb@city.ac.uk).

P. G. Schlottmann was with NIHR Biomedical Research Centre for Ophthalmology, Moorfields Eye Hospital NHS Foundation Trust and UCL Institute of Ophthalmology, 162 City Road, London, EC1V 2PD, UK (e-mail: schlottp@yahoo.com.ar).

G. Wollstein is with Eye Center of University of Pittsburgh Medical Center (UPMC), Department of Ophthalmology, University of Pittsburgh School of Medicine, 203 Lothrop Street, Eye and Ear Institute, Suite 834, Pittsburgh, PA 15213, USA (e-mail: wollsteing@upmc.edu).

D. F. Garway-Heath is with NIHR Biomedical Research Centre for Ophthalmology, Moorfields Eye Hospital NHS Foundation Trust and UCL Institute of Ophthalmology, 162 City Road, London, EC1V 2PD, UK (email: david.garway-heath@moorfields.nhs.uk).

I. INTRODUCTION

GLAUCOMA is a leading cause of irreversible visual impairment, being a progressive optic neuropathy resulting in the loss or damage of retinal ganglion cells (RGCs) and their axons. In human eyes, light rays are focused and sensed on the retina, which is the tissue layer at the back of the eye. Simply put, the top 'layer' of the retina consists of retinal ganglion cells and their axons (nerve fibres) with photoreceptors (rods and cones) underneath. The retinal nerve fibres converge to form the optic nerve head (ONH) where they exit the eye to enter the brain. The retinal nerve fibres carry the signals from across the retina into the brain so the damage or 'thinning' of RGCs and their axons caused by glaucoma results in the irreversible visual impairment.

Estimates of RGC axon loss can be made by the surrogate measurement of retinal nerve fibre layer (RNFL) thickness using modern imaging techniques such as optical coherence tomography (OCT) [1, 2]. Similar to ultrasound technique, OCT detects the backscattered light from the retina and produces high resolution, cross-sectional images. This technique has formed time-domain OCT (TD-OCT) systems such as the StratusOCT (Carl Zeiss Meditec, Inc., Dublin, CA) that has been successfully used in the clinic as a clinical standard for measuring the RNFL thickness (RNFLT) in glaucoma in recent years [3-7]. In the StratusOCT system measurement of the retinal layers is acquired by an axial-scan in depth (A-scan) and a cross-sectional scan (B-scan). The A-scans are sampled under a scan circle (typical diameter of 3.4 mm) which is manually centred on the optic nerve head (ONH; Figure 1(I)) as guided by a 'live' image of the fundus but the location of the scan circle is unknown during the image acquisition. The RNFLT is then analysed by segmentation algorithms provided by the software. One difficulty during image acquisition is the displacement of the circular scan due to the operator's subjective placement of the scan circle or the eye movement after the manual adjustment. This displacement means that the RNFLT is not necessarily sampled at the same location and this contributes to the variability and error in the measurement [8-10], restricting the use of the technique especially in determining the deterioration of the RNFLT in the longitudinal assessment or follow-up of glaucoma. Moreover, the problem of RNFLT reproducibility due to image acquisition difficulties was also recently identified as a

limiting factor for this technology in the diagnosis or management of multiple sclerosis [11]. Therefore, a method for identifying and aligning the location of the scan circle would be clinically useful as it may offer better tracking of the same area of RNFLT over time.

Newer spectral-domain OCT (SD-OCT) [12, 13] operates with faster scans [14] giving improved signal-to-noise ratio in the measurements [15, 16] compared to TD-OCT. Although some commercially available SD-OCT (e.g. Cirrus, Carl Zeiss Meditec, CA, USA) scan protocols extract the circular scan from 3D volume scan, most other SD-OCT systems (e.g. RTVue-100, Optovue, Fremont, CA, USA) still provide circular scan as one of the scan protocols or include circular scans in more complex protocols (e.g. RTVue-100 NHM4 protocol consisting of 6 circle and 12 line scans) so they may still be affected by displacement between scans [8, 17]. Therefore, improvements in this image acquisition protocol, or at least knowing the area of RNFLT that has been acquired, will still be beneficial for SD-OCT devices with such scan acquisition protocols. Moreover, TD-OCT has been used to follow up the progression of glaucoma long before the emergence of the SD-OCT, and it is still widely used by glaucoma services where clinicians (or research study co-ordinators) are reluctant to abandon series of data collected with TD-OCT over time since this provides important information about the longitudinal characteristic of glaucoma. The method proposed in this study may facilitate migration from TD-OCT to SD-OCT, for instance, by aligning TD-OCT scan circles on the volumetric images acquired by SD-OCT, so that longitudinal series are not wasted.

The effect of scan circle location on the RNFLT measurement has been previously investigated by simulating different scan circle locations on a volumetric image around the ONH taken by ultrahigh-resolution OCT [8]. The circular scans were simulated by sampling the A-scans under a scan circle (3.4 mm diameter) shifted with known displacements horizontally (x-shift), vertically (y-shift) and diagonally from the centre of the ONH. This method allowed for systematic investigation of the variable circle placement effect. The results from this study clearly demonstrated that location of the OCT scan circle adds substantial variability to the RNFLT measurements. Since registration of OCT scans is imperative for measurement reproducibility and longitudinal examination it would be very useful to have a method that could estimate the location of the scan circle on the retina. Kim et al. [18] proposed a method to align the circular scan image to a volumetric image around the ONH acquired by SD-OCT by using simulated cross-sectional images under scan circles at various locations sampled from the volumetric image. The circular scan was then aligned to the most similar sampled SD-OCT scans where the similarity was assessed by cross correlation between retinal structures in the A-scans from two images. One limitation is that the technique uses retinal structures that typically change during the worsening of glaucoma, giving it limited appeal in following up RNFLT changes if the circular scan and volumetric scans are acquired in different periods of time. This approach might help bridge the gap in RNFLT measurements between the TD-OCT circular scan and SD-OCT volumetric scan, providing longitudinal comparability. However this approach is only useful when both TD-OCT and SD-OCT are available and it will not be helpful in a common situation where a clinic might be following patients with TD-OCT technology alone for years.

This study proposes a new OCT scan circle alignment algorithm using blood vessel features which are considered to be relatively stable landmarks when considering longitudinal images in glaucoma. The algorithm can align multiple OCT circular scans to a retinal fundus image that is generally available in the glaucoma clinics from various imaging techniques, such as scanning laser polarimetry (SLP), scanning laser ophthalmoscope or even a fundus camera. The algorithm has been developed to have general applicability to any type of fundus and OCT images but is demonstrated in this study on StratusOCT images using fundus images acquired with SLP (GDxVCC; Carl Zeiss Meditec, Inc., Dublin, CA, USA). It has been successfully used in a recent study that assessed the axonal birefringence of RNFL by aligning the OCT scan circle onto the SLP image [19].

II. METHODS

The proposed method aligns an OCT scan circle on the retinal fundus image by a registration technique using the blood vessel features available in both types of images. The vessels in OCT images typically appear as shaded bands along the retinal pigment epithelium (RPE; Figure 1(II)). The RPE is detected as the tissue layer with the strongest intensity peaks in the OCT image. The 'shaded band' feature of vessels is then detected as the local minimums on the averaged pixel intensities around the RPE (Figure 1(II)). The vessel features in the retinal fundus images differ with the imaging techniques used, and the vessel segmentation in retinal images have been extensively studied previously [20-25]. In the implementation of vessel detection for SLP fundus image, a measure of 'vesselness' serves as a pre-processing step for segmentation of vessels in the retinal fundus image. A technique using the multi-scale second order local structure of an image (Hessian) [26] is used for this purpose. The vessels are then analytically reconstructed using cubic splines (Figure 1(I)) [27].

A scan circle around the ONH and the detected vessels in the OCT (white circles superimposed on the blue scan circle) and fundus image (red lines) are shown in Figure 1. That the scan circle is displaced is indicated by the poorly aligned vessels. The method proposed in this work infers the scan circle location by aligning the vessels from both images.

A. Problem formalisation

In an acquisition of an OCT image (Figure 1), the circular scan starts from the mid-temporal area at 180° (blue arrow on scan circle in Figure 1(I) and traverses in a clock-wise direction to superior (90°), nasal (0°), inferior (-90°) and finally back to the mid-temporal area. The circular scan is then

'straightened' to a 'line' in two dimensions (Figure 1(II)). Each column in the OCT image is therefore associated with an angular value on the scan circle. The locations of detected vessels in the OCT image are converted to angular values (e.g. Figure 1(III)) and are denoted as $\left\{ \mathbf{X}_i \right\}_{i=1}^N$ where N is the number of OCT vessels. The x- and y-coordinates of each vessel in the retinal fundus image are expressed as two cubic splines [27] respectively, each of which is essentially a piecewise function defined over a parameter u. The cubic spline has H-1 segments divided by H knots $(u_1,..., u_H)$ on u and the one having an intersection with the scan circle is assumed to be the hth segment, so the coordinate (x_{jh}, y_{jh}) of this segment of the jth fundus image vessel are:

$$\begin{cases} x_{jh} = a_{jxh}(u-u_h)^3 + b_{jxh}(u-u_h)^2 + c_{jxh}(u-u_h) + d_{jxh} \\ y_{jh} = a_{jyh}(u-u_h)^3 + b_{jyh}(u-u_h)^2 + c_{jyh}(u-u_h) + d_{jyh} \end{cases} \quad (1)$$

The location of a scan circle with radius r=3.4mm is defined by three parameters: centre coordinate (s, t), and rotation θ (in degree) around the centre. The circle rotation θ rotates all OCT vessels around the scan circle centre by θ degrees and, in the 'straightened' two dimensions image (Figure 1(II)), it shifts the OCT vessels (and the whole image) on horizontal by θ degrees. Given the parameters of a scan circle, the intersection between a vessel defined by Equation (1) and the scan circle can be calculated by solving the following polynomial equation with respect to u:

$$\left[a_{jxh}(u-u_h)^3 + b_{jxh}(u-u_h)^2 + c_{jxh}(u-u_h) + d_{jxh} - s \right]^2$$
$$+ \left[a_{jyh}(u-u_h)^3 + b_{jyh}(u-u_h)^2 + c_{jyh}(u-u_h) + d_{jyh} - t \right]^2 = r^2 \quad (2)$$

with the constraint $u_h \leq u < u_{h+1}$ and inserting the root $\hat{u}$ back to Equation (1) to calculate the solutions of $\hat{x}_{jh}$ and $\hat{y}_{jh}$. The angular value of the intersection is then calculated as:

$$f_j(s, t, \theta) = \begin{cases} \tan^{-1}\left(\dfrac{\hat{y}_{jh} - t}{\hat{x}_{jh} - s} \right) + \theta & \hat{x}_{jh} \geq s \\ \tan^{-1}\left(\dfrac{\hat{y}_{jh} - t}{\hat{x}_{jh} - s} \right) + \theta + 180° & \hat{x}_{jh} < s,\ \hat{y}_{jh} \geq t \\ \tan^{-1}\left(\dfrac{\hat{y}_{jh} - t}{\hat{x}_{jh} - s} \right) + \theta - 180° & \hat{x}_{jh} < s,\ \hat{y}_{jh} < t \end{cases} \quad (3)$$

for $\left\{ f_j(s, t, \theta) \right\}_{j=1}^M$ where M is the number of vessels in the fundus image. $f_j(s, t, \theta)$ is also used to represent the corresponding fundus image vessel.

The scan circle alignment can be decomposed into two tasks: vessel matching and displacement parameter inference. The vessel matching links an OCT vessel $\mathbf{X}_i$ and a fundus image vessel $f_j(s, t, \theta)$ if they belong to a same vessel. The displacement parameter inference infers the parameters (s, t) and θ to minimise the distances between the matched vessels in two images. These two steps are both non-trivial and affect each other in a complex way. For instance, the OCT and fundus image vessels in Figure 1 cannot be matched without knowing the location parameters. An OCT vessel cannot be simply matched to the nearest fundus image vessel. In the example in Figure 1, the nearest-matching criterion (Figure 1(III)) results in obvious erroneous vessel pairs (c-C, f-J, i-M and j-N in Figure 1(I)). On the other hand, the displacement parameters cannot be inferred without knowing how the vessels in two images are matched. Because of the complicated interaction between vessel matching and parameter inference, treating them independently would result in suboptimal solutions.

Figure 1. A retinal fundus image and OCT circular scan for the same eye. The detected vessels are modelled and delineated by cubic splines, shown here as red curves superimposed on the fundus image (I) and labelled with letters in uppercase (A to N). The image acquisition begins with a circle placed in an arbitrary position around the ONH, e.g. the blue line in (I). The scan starts from the mid-temporal area at 180° (blue arrow on scan circle) and traverses in a clock-wise direction to superior (90°), nasal (0°), inferior (-90°) and finally back to the mid-temporal area. The circular scan is 'straightened' to a line (in 2D) as shown in

(II). The results of the OCT vessel detection technique are indicated in (II) as crosses and are superimposed as white circles in the fundus image (I). The OCT vessels are numbered by letters in lowercase (a to j). The angular values of the indicated position of the OCT vessels and the intersections between the scan circle and fundus image vessels are plotted in (III). The lines in (III) link each OCT vessel to the nearest fundus image vessel.

B. Probabilistic modelling

The complex relationship between the vessel matching and scan circle displacement parameter inference is modelled with a probabilistic model with unobserved variable. The task of vessel matching can be divided into two processes. First, whether the OCT vessel $\mathbf{X}_i$ can be matched to a fundus image vessel is examined. If this can be done accurately then an inference about what M vessels in the fundus image it needs to be matched to. Two groups of unobserved variables are introduced to model these two processes. The binary vector $\left\{ \mathbf{Y}_i = \left(\mathbf{Y}_{i0}, \mathbf{Y}_{i1} \right) \right\}_{i=1}^{N}$ is encoded with 1-out-of-2 notation in which only one of the two elements can be equal to 1 in $\mathbf{Y}_i$: $\mathbf{Y}_{i1} = 1$ if the ith OCT vessel $\mathbf{X}_i$ can be accurately aligned to a fundus image vessel, otherwise $\mathbf{Y}_{i0} = 1$. A prior probability over $\mathbf{Y}_i$ is introduced such that $P\left(\mathbf{Y}_{ik} = 1 \right) = \mathbf{u}_k$ for $k = 0$ or 1 so:

$$P\left(\mathbf{Y}_i \right) = \prod_{k=0}^{1} \left(\mathbf{u}_k \right)^{\mathbf{Y}_{ik}} \qquad (4)$$

It is also required that probability values satisfy $\sum_{k=0}^{1} \mathbf{u}_k = 1$.

Another binary vector $\left\{ \mathbf{Z}_i = \left(\mathbf{Z}_{i1}, ..., \mathbf{Z}_{iM} \right) \right\}_{i=1}^{N}$ adopts 1-out-of-M notation so that only one of the M elements in $\mathbf{Z}_i$ can be equal to 1, and $\mathbf{Z}_{ij} = 1$ indicates that the ith OCT vessel is matched to the jth fundus image vessel. Similarly, a prior probability over $\mathbf{Z}_i$ is set as $P\left(\mathbf{Z}_{ij} = 1 \right) = \boldsymbol{\pi}_j$ for $k = 1$ to M so:

$$P\left(\mathbf{Z}_i \right) = \prod_{j=1}^{M} \left(\boldsymbol{\pi}_j \right)^{\mathbf{Z}_{ij}} \qquad (5)$$

where $\left\{ \boldsymbol{\pi}_j \right\}_{j=1}^{M}$ are probability values satisfying $\sum_{j=1}^{M} \boldsymbol{\pi}_j = 1$.

The posterior probability of $\mathbf{X}_i$ given $\mathbf{Z}_{ij} = 1$ is defined as a mixture of two Gaussian distributions centred on the same mean of $f_j\left(s, t, \theta \right)$ but with different variance δ_k^2 that is decided by the value of $\mathbf{Y}_i$:

$$P(\mathbf{X}_i \mid \mathbf{Y}_i, \mathbf{Z}_{ij} = 1) = \prod_{k=0}^{1} \left(\mathcal{N}\left(\mathbf{X}_i \mid f_j\left(s, t, \theta \right), \delta_k^2 \right) \right)^{\mathbf{Y}_{ik}} \qquad (6)$$

where the parameters $\left\{ \delta_k^2 \right\}_{k=0}^{1}$ are set to satisfy $\delta_1^2 \ll \delta_0^2$. This can be interpreted as if the OCT vessel $\mathbf{X}_i$ can be accurately aligned to the fundus image vessel $f_j\left(s, t, \theta \right)$ ($\mathbf{Y}_{i1} = 1$), then $\mathbf{X}_i$ needs to be close to $f_j\left(s, t, \theta \right)$ in order to 'score' a high probability, otherwise a small divergence (defined by small δ_1 such as 2°) from $f_j\left(s, t, \theta \right)$ would result in a probability near to zero. On the other hand, if the

OCT vessel $\mathbf{X}_i$ cannot be accurately aligned to a fundus image vessel ($\mathbf{Y}_{i0} = 1$), $\mathbf{X}_i$ distributes more 'uniformly' (defined by large δ_0 such as 45°) with a small probability value, so the divergence from $f_j\left(s, t, \theta \right)$ has minimal effect on the probability.

From Equation (6), the posterior probability $P\left(\mathbf{X}_i \mid \mathbf{Y}_i, \mathbf{Z}_i \right)$ can be defined as:

$$P\left(\mathbf{X}_i \mid \mathbf{Y}_i, \mathbf{Z}_i \right) = \prod_{j=1}^{M} \left(\prod_{k=0}^{1} \mathcal{N}\left(\mathbf{X}_i \mid f_j\left(s, t, \theta \right), \delta_k^2 \right)^{\mathbf{Y}_{ik}} \right)^{\mathbf{Z}_{ij}} \qquad (7)$$

from which the joint probability $P\left(\mathbf{X}_i, \mathbf{Y}_i, \mathbf{Z}_i \right)$ can be calculated as the multiplication of Equation (4), (5) and (7):

$$P(\mathbf{X}_i, \mathbf{Y}_i, \mathbf{Z}_i) = \prod_{j=1}^{M} \left(\boldsymbol{\pi}_j \prod_{k=0}^{1} \left(\mathbf{u}_k \mathcal{N}\left(\mathbf{X}_i \mid f_j\left(s, t, \theta \right), \delta_k^2 \right) \right)^{\mathbf{Y}_{ik}} \right)^{\mathbf{Z}_{ij}} \qquad (8)$$

The joint probability $P\left(\mathbf{X}_i, \mathbf{Y}_i, \mathbf{Z}_i \right)$ defines a mixture of Gaussian mixture. This 'mixture of mixture' model structure was previously used for classification problems [28] and in other applications where the model was named after 'compound mixture model' [29].

Because $\left\{ \mathbf{Y}_i \right\}_{i=1}^{N}$ and $\left\{ \mathbf{Z}_i \right\}_{i=1}^{N}$ are all unobserved variables as opposed to directly observed variables, the likelihood can be calculated by marginalising the joint probability over these unobserved variables and assuming that $\left\{ \mathbf{X}_i \right\}_{i=1}^{N}$ are independent and identically distributed:

$$\begin{aligned} P(\mathbf{X}) &= \prod_{i=1}^{N} \sum_{\mathbf{Y}_i, \mathbf{Z}_i} \prod_{j=1}^{M} \left(\boldsymbol{\pi}_j \prod_{k=0}^{1} \left(\mathbf{u}_k \mathcal{N}\left(\mathbf{X}_i \mid f_j\left(s, t, \theta \right), \delta_k^2 \right) \right)^{\mathbf{Y}_{ik}} \right)^{\mathbf{Z}_{ij}} \\ &= \prod_{i=1}^{N} \left[\sum_{j=1}^{M} \boldsymbol{\pi}_j \sum_{k=0}^{1} \mathbf{u}_k \mathcal{N}\left(\mathbf{X}_i \mid f_j\left(s, t, \theta \right), \delta_k^2 \right) \right] \end{aligned} \qquad (9)$$

Because only one element in vectors $\mathbf{Y}_i$ and $\mathbf{Z}_i$ can be equal to '1' respectively, the summation $\sum_{\mathbf{Y}_i, \mathbf{Z}_i}$ and multiplication over j and k in the first step of Equation (9) represent the exhaustive summation of all possible $\boldsymbol{\pi}_j \mathbf{u}_k \mathcal{N}\left(\mathbf{X}_i \mid f_j\left(s, t, \theta \right), \delta_k^2 \right)$ over j and k. Therefore, in the second step, $\sum_{\mathbf{Y}_i, \mathbf{Z}_i}$ and the multiplication over j and k were substituted with summation over j and k.

C. Expectation-maximization algorithm

An *expectation-maximization* (EM) algorithm [30] is used for finding maximum likelihood estimates of the parameters in Equation (9). In the *expectation* (E) step, the posterior probability of the unobserved variables $P\left(\mathbf{Y}_i, \mathbf{Z}_i \mid \mathbf{X}_i \right)$ is calculated as:

$$P(\mathbf{Y}_i, \mathbf{Z}_i \mid \mathbf{X}_i) = \frac{P(\mathbf{X}_i, \mathbf{Y}_i, \mathbf{Z}_i)}{P(\mathbf{X}_i)}$$

$$= \frac{\prod_{j=1}^{M} \left(\boldsymbol{\pi}_j \prod_{k=0}^{1} \left(\mathbf{u}_k \mathcal{N} \left(\mathbf{X}_i \mid f_j(s, t, \theta), \delta_k^2 \right) \right)^{\mathbf{Y}_{ik}} \right)^{\mathbf{Z}_{ij}}}{\sum_{j=1}^{M} \boldsymbol{\pi}_j \sum_{k=0}^{1} \mathbf{u}_k \mathcal{N} \left(\mathbf{X}_i \mid f_j(s, t, \theta), \delta_k^2 \right)} \quad (10)$$

by using Equation (8) and the *i*th component in Equation (9). The expectations of $\mathbf{Z}_{ij}$ and $\mathbf{Z}_{ij}\mathbf{Y}_{ik}$ w.r.t. the distribution $P(\mathbf{Y}_i, \mathbf{Z}_i \mid \mathbf{X}_i)$ are then calculated in the E-step and will be used in the following *maximization* (M) step, which computes parameters maximising the expected log likelihood found in the E step:

$$\boldsymbol{\alpha}_{ij} = \mathrm{E}_{P(\mathbf{Y}_i, \mathbf{Z}_i \mid \mathbf{X}_i)}\left(\mathbf{Z}_{ij}\right) = P(\mathbf{Z}_{ij} = 1 \mid \mathbf{X}_i)$$

$$= \frac{\boldsymbol{\pi}_j \sum_{k=0}^{1} \mathbf{u}_k \mathcal{N} \left(\mathbf{X}_i \mid f_j(s, t, \theta), \delta_k^2 \right)}{\sum_{j=1}^{M} \boldsymbol{\pi}_j \sum_{k=0}^{1} \mathbf{u}_k \mathcal{N} \left(\mathbf{X}_i \mid f_j(s, t, \theta), \delta_k^2 \right)} \quad (11)$$

and

$$\boldsymbol{\beta}_{ij}^k = \mathrm{E}_{P(\mathbf{Y}_i, \mathbf{Z}_i \mid \mathbf{X}_i)}\left(\mathbf{Z}_{ij}\mathbf{Y}_{ik}\right) = P(\mathbf{Y}_{ik} = 1, \mathbf{Z}_{ij} = 1 \mid \mathbf{X}_i)$$

$$= \frac{\boldsymbol{\pi}_j \mathbf{u}_k \mathcal{N} \left(\mathbf{X}_i \mid f_j(s, t, \theta), \delta_k^2 \right)}{\sum_{j=1}^{M} \boldsymbol{\pi}_j \sum_{k=0}^{1} \mathbf{u}_k \mathcal{N} \left(\mathbf{X}_i \mid f_j(s, t, \theta), \delta_k^2 \right)} \quad (12)$$

In the M-step, the expectation of the complete likelihood $\log\left(P(\mathbf{X}, \mathbf{Y}, \mathbf{Z})\right)$ under the distribution of $P(\mathbf{Y}, \mathbf{Z} \mid \mathbf{X})$ is calculated and maximised w.r.t. the parameters (s, t), θ, $\{\mathbf{u}_k\}_{k=0}^{1}$ and $\{\boldsymbol{\pi}_j\}_{j=1}^{M}$:

$$\mathrm{E}_{P(\mathbf{Y}, \mathbf{Z} \mid \mathbf{X})}\left(\log\left(P(\mathbf{X}, \mathbf{Y}, \mathbf{Z})\right)\right)$$

$$= \sum_{i=1}^{N}\sum_{j=1}^{M} \mathrm{E}\left(\mathbf{Z}_{ij}\right)\log(\boldsymbol{\pi}_j) + \sum_{i=1}^{N}\sum_{j=1}^{M}\sum_{k=0}^{1} \mathrm{E}\left(\mathbf{Z}_{ij}\mathbf{Y}_{ik}\right)\log(\mathbf{u}_k)$$

$$+ \sum_{i=1}^{N}\sum_{j=1}^{M}\sum_{k=0}^{1} \mathrm{E}\left(\mathbf{Z}_{ij}\mathbf{Y}_{ik}\right)\log\left(\mathcal{N}\left(\mathbf{X}_i \mid f_j(s, t, \theta), \delta_k^2\right)\right)$$

$$= \sum_{i=1}^{N}\sum_{j=1}^{M} \boldsymbol{\alpha}_{ij}\log(\boldsymbol{\pi}_j) + \sum_{i=1}^{N}\sum_{j=1}^{M}\sum_{k=0}^{1} \boldsymbol{\beta}_{ij}^k\log(\mathbf{u}_k)$$

$$- \frac{1}{2}\sum_{i=1}^{N}\sum_{j=1}^{M}\sum_{k=0}^{1} \frac{\boldsymbol{\beta}_{ij}^k \left(\mathbf{X}_i - f_j(s, t, \theta)\right)^2}{\delta_k^2} + const \quad (13)$$

where Equation (11) and (12) have been used. This target function is divided into three components each of which contains a group of the parameters. Note that the components of this function that do not include any parameters were grouped into a constant term as they are irrelevant to the maximisation of the objective function.

Similar to the mixture of Gaussian mixture model [28] and compound mixture model [29], the Equation (13) is maximized w.r.t. parameters $\{\boldsymbol{\pi}_j\}_{j=1}^{M}$ under the constraint of $\sum_{j=1}^{M}\boldsymbol{\pi}_j = 1$ by adding a *Lagrange* multiplier $\lambda_{\boldsymbol{\pi}}\left(\sum_{j=1}^{M}\boldsymbol{\pi}_j - 1\right)$ into Equation (13) and setting the derivative of the objective

function w.r.t. $\boldsymbol{\pi}_j$ to 0:

$$\boldsymbol{\pi}_j = \frac{\sum_{i=1}^{N}\boldsymbol{\alpha}_{ij}}{N} \quad (14)$$

Similarly, $\{\mathbf{u}_k\}_{k=0}^{1}$ are found by using the *Lagrange* multiplier $\lambda_{\mathbf{u}}\left(\sum_{k=0}^{1}\mathbf{u}_j - 1\right)$:

$$\mathbf{u}_k = \frac{\sum_{i=1}^{N}\sum_{j=1}^{M}\boldsymbol{\beta}_{ij}^k}{N} \quad (15)$$

The optimization of Equation (13) w.r.t. parameters (s, t), and θ is more complex because setting the derivative of Equation (13) w.r.t. these parameters to zero does not give a closed solution for these parameters. Therefore, the iterative Quasi-Newton optimization algorithm [31] is used to find the maxima of the third component in Equation (13)

$$\mathrm{E} = -\frac{1}{2}\sum_{i=1}^{N}\sum_{j=1}^{M}\sum_{k=0}^{1} \frac{\boldsymbol{\beta}_{ij}^k \left(\mathbf{X}_i - f_j(s, t, \theta)\right)^2}{\delta_k^2} \quad (16)$$

w.r.t. (s, t), and θ in every M-step. Quasi-Newton algorithm is based on Newton's method [32, 33] that uses the first and second derivatives (gradient vector and Hessian matrix) to find the local maximum. Instead of explicitly calculating the Hessian matrix, which is computationally expensive, Quasi-Newton avoids the exact computation of the second derivatives and updates the Hessian matrix by analysing successive gradient vectors [31, 33]. This allows the Quasi-Newton algorithm to be implemented with computational efficiency and consequently forms an efficient M-step in the EM algorithm. The Quasi-Newton algorithm makes use of the gradient of the Equation (16) w.r.t. (s, t), and θ, which can be simply derived from Equation (1), (2) and (3) by using the chain rule of the derivative. Quasi-Newton algorithm stops when the following parameter convergence criteria are met: 1) the absolute difference between the values of (s, t) between two successive iterations is less than 10^{-5}μm; and 2) the absolute difference between the values of θ between two successive iterations is less than 10^{-5} degrees.

In all, the EM algorithm starts with initial values of the parameters (s, t), θ, $\{\mathbf{u}_k\}_{k=0}^{1}$ and $\{\boldsymbol{\pi}_j\}_{j=1}^{M}$ and iterates between the E-step and M-step. The whole process of the algorithm is summarized in Figure 2. The parameter (s, t), θ, $\{\mathbf{u}_k\}_{k=0}^{1}$ and $\{\boldsymbol{\pi}_j\}_{j=1}^{M}$ are initialised at the beginning of the algorithm. More details about initialisation will be given in the next section. In the E-step, $\boldsymbol{\alpha}_{ij}$ and $\boldsymbol{\beta}_{ij}^k$ in Equation (11) and (12) are calculated using the current parameter values: initialized parameters in the first iteration or the parameters formed by the M-step in the previous iteration afterwards. In the M-step, $\boldsymbol{\alpha}_{ij}$ and $\boldsymbol{\beta}_{ij}^k$ calculated in the E-step are used and

the expected complete log likelihood in Equation (13) is maximized using Equation (14), (15) and Quasi-Newton optimization to form the new estimate of parameters $\left(s^{new},\ t^{new}\right)$ and θ^{new} that will be used in the next E-step. The iteration terminates if the scan circle falls outside of the borders of the fundus image or when the following parameter convergence criteria are met: 1) the absolute difference between the values of $(s,\ t)$ between two successive EM iterations is less than $10^{-5}\mu\text{m}$; 2) the absolute difference between the values of θ between two successive EM iterations is less than 10^{-5} degrees; 3) the absolute difference between the values of $\left\{\mathbf{u}_k\right\}_{k=0}^{1}$ and $\left\{\boldsymbol{\pi}_j\right\}_{j=1}^{M}$ between two successive EM iterations is less than 10^{-6}.

Initialize parameters:
e.g., $(s,\ t) =$ optic nerve head centre, $\theta = 0$,
$\mathbf{u}_1 = 0.95$, $\mathbf{u}_0 = 0.05$, $\left\{\boldsymbol{\pi}_j\right\}_{j=1}^{M} = \dfrac{1}{M}$

E-step: calculate $\boldsymbol{\alpha}_{ij}$ and $\boldsymbol{\beta}_{ij}^{k}$ using Equation (11) and (12) with the current parameter values

M-step: with $\boldsymbol{\alpha}_{ij}$ and $\boldsymbol{\beta}_{ij}^{k}$ from the E-step, re-estimate the parameters $\left\{\boldsymbol{\pi}_j^{\ new}\right\}_{j=1}^{M}$ and $\left\{\mathbf{u}_k^{\ new}\right\}_{k=0}^{1}$ using Equation (16) and (17). Re-estimate the parameters $\left(s^{new},\ t^{new}\right)$, θ^{new} by maximizing Equation (18) using Quasi-Newton algorithm. Update the current parameter values with the new re-estimats.

Not converge

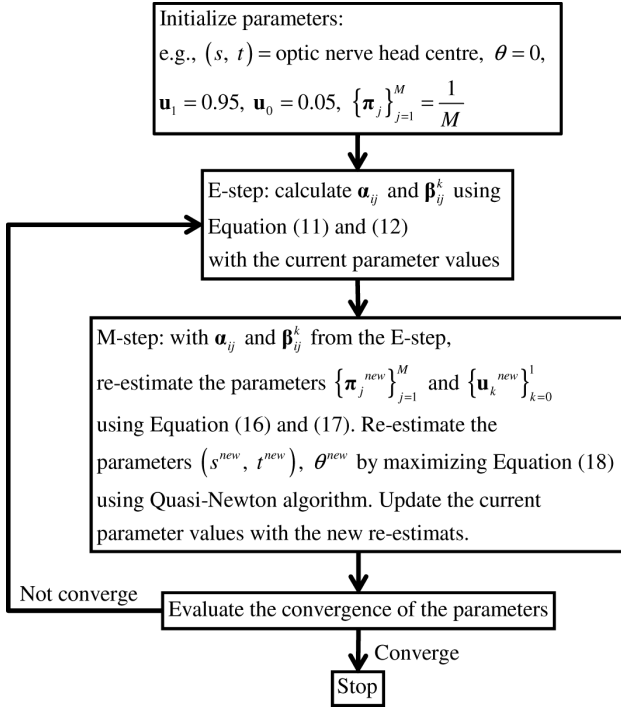Evaluate the convergence of the parameters

Converge

Stop

Figure 2. A summary of the EM algorithm.

D. Evaluation and parameter initialisation

The algorithm was evaluated using the mean absolute angular difference (MAAD) between the matched vessels in the OCT and fundus images. The vessel matching is determined by the probability $P\left(\mathbf{Y}_i\,|\,\mathbf{X}_i\right)$ and $P\left(\mathbf{Z}_i\,|\,\mathbf{X}_i\right)$, which can be calculated from $P\left(\mathbf{Y}_i,\ \mathbf{Z}_i\,|\,\mathbf{X}_i\right)$ in Equation (10) by marginalization after the termination of the algorithm. The ith OCT vessel is aligned to the jth fundus image vessel if $P\left(\mathbf{Y}_{i1} = 1\,|\,\mathbf{X}_i\right) > P\left(\mathbf{Y}_{i0} = 1\,|\,\mathbf{X}_i\right)$ and $P\left(\mathbf{Z}_{ij} = 1\,|\,\mathbf{X}_i\right)$ is the largest among $P\left(\mathbf{Z}_{ij'}\,|\,\mathbf{X}_i\right)$ for $j' = 1$ to M. In the unlikely case that multiple OCT vessels are so close that they are matched to the same fundus image vessel, only the OCT vessel closest to the fundus image vessel is matched. The vessel matching guarantees that the same number of vessels is matched in both OCT and fundus images so those matched vessels in two types of images form vessel pairs. The MAAD is then calculated as the mean of the absolute angular difference between these vessel pairs.

The criteria for a successful inference include: 1) $\mathbf{u}_1 \geq 0.7$; 2) the number of matched vessels is larger than 5; 3) the MAAD between the matched vessels is smaller than δ_1 which is set at 2° in the implementation with δ_0 set at 45°. The choice of δ_1 and δ_0 will be explained in next section; 4) the inferred scan circle is within the border of fundus image. The first two criteria ensure that the inferred scan circle displacement is 'agreed' by adequate number of vessels. The third criterion guarantees that the distance between the matched vessels is sufficiently small.
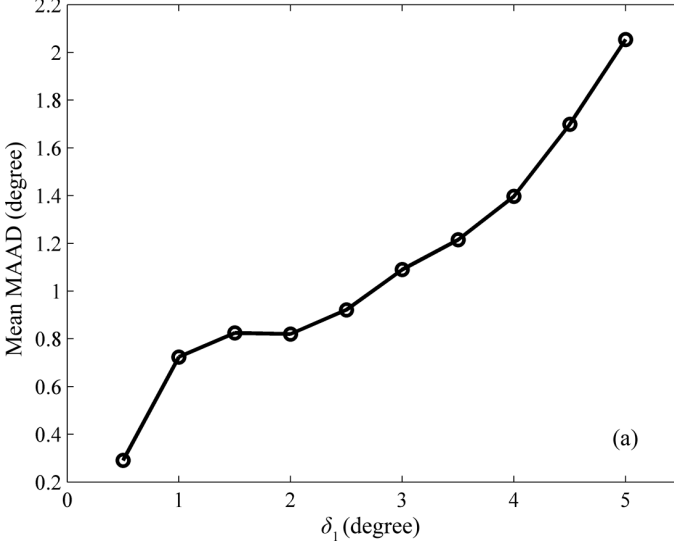
Without losing generalisation, the parameters θ, $\left\{\mathbf{u}_k\right\}_{k=0}^{1}$ and $\left\{\boldsymbol{\pi}_j\right\}_{j=1}^{M}$ are initialised to be $\theta = 0^{\circ}$, $\mathbf{u}_1 = 0.95$, $\mathbf{u}_0 = 0.05$ and $\boldsymbol{\pi}_j = \dfrac{1}{M}$. The choice of $\mathbf{u}_1 = 0.95$ results from the expectation that most OCT vessels can be aligned to the fundus image vessels. There are multiple initialisation options for the parameters $(s,\ t)$ in order to cope with the potential large displacement of scan circles: they are initialised to be at nine locations shifted by 0 and $\pm 200\mu\text{m}$ from the centre of the ONH on both the x- and y-axis. The algorithm starts with different parameter initialisation and if the inferred values of parameters are different with different initialization, the displacement is chosen as the one with the lowest MAAD from a successful inference.

E. Choice of δ_1 and δ_0

The parameters δ_1 and δ_0 were set such that $\delta_1 << \delta_0$. Quantitatively, it was defined that the two intersections between the two Gaussian distributions defined by δ_1 and δ_0 in Equation (6) are $2.5\delta_1$ from the mean. Therefore, given the value of δ_1, δ_0 can be calculated thereafter. To find the optimal δ_1, various values of δ_1 are used and the mean MAAD and mean $\mathbf{u}_1$ are examined (Figure 3). To illustrate the effect of δ_1, the first two criteria of successful inference are not used because, as it will be shown below, fewer ($\mathbf{u}_1 < 0.7$) OCT vessels can be matched to the fundus image vessels with small δ_1 values.

δ_1 defines the necessary 'closeness' of the OCT vessel to the fundus image vessel in order to match the two vessels. As shown in Figure 3(a), small δ_1 allows for a smaller difference between the OCT and fundus image vessels and thus gives better (lower) MAAD for the matched vessels. However, smaller δ_1 also excludes more OCT vessels so fewer OCT vessels can be matched to the fundus image vessels, which is

quantified by lower value of $\mathbf{u}_1$ (Figure 3(b)). For instance, although $\delta_1 = 0.5^o$ gives a low mean MAAD of 0.29°, but less than 70% ($\mathbf{u}_1 < 0.59$) of the OCT vessels can be matched to the fundus image vessels. On the other hand, large δ_1 allows for more OCT vessels to be matched to the fundus image vessels but the MAAD also increases at the same time.

Therefore, the choice of δ_1 reflects the trade-off between lower MAAD and having adequate number of matched vessels. In this implementation, δ_1 is chosen as the value giving the lowest mean MAAD with mean $\mathbf{u}_1 \geq 0.7$ as required by the criteria of successful inference. This value of δ_1 was found to be 2°, and δ_0 is calculated to be 45°.

Figure 3. The mean MAAD and $\mathbf{u}_1$ under different values of δ_1.

F. Validation experiments

The OCT scan circle alignment algorithm was developed and implemented in MATLAB (version 7.9.0 R2009b, The MathWorks, Inc., Natick, MA). An executable version of this software is freely available from the authors.

The algorithm was initially developed using Stratus OCT data from patients with glaucoma made available from the Eye Center of University of Pittsburgh Medical Centre (data not shown) [18, 34]. The algorithm was then validated by investigating the impact of scan circle displacement on the RNFLT measurement repeatability using a separate dataset acquired for the purpose from Moorfields Eye Hospital NHS Trust, London. Eighteen patients (mean age of 65 (range 50 to 82) years) with a clinical diagnosis of glaucomatous optic neuropathy (primary open angle or normal tension glaucoma) with reproducible visual field defects were recruited. The study was approved by an ethics committee and informed consent, according to the tenets of the Declaration of Helsinki, was obtained prior to examination from each subject. In the study protocol, a chosen eye from each subject was imaged 23 times with the StratusOCT system using the Fast RNFL Thickness (3.4) protocol. This protocol acquired three consecutive single scans in one image acquisition giving 69 single scans for each eye. Fundus images were acquired with the GDxVCC which covers an area of 5.9mm×5.9mm around the ONH. Patient identifiers were removed from the data before being transferred to a secure database at City University London.

III. RESULTS

The algorithm was used to align all 69 OCT circular scans onto the corresponding fundus images for each eye. On average, the EM algorithm took 10.3 iterations before convergence. In each M-step, the average number of Quasi-Newton optimisation was 23.2. Computational time for aligning each OCT scan circle to the fundus image was 2.3s (SD 0.6s) on a typical desktop PC with one core of Intel Core 2 Due 2.53GHz CPU and 2GB RAM.

A. Algorithm performance

An example of the results from the alignment algorithm for one of the eyes is shown in Figure 4. The initial location of the OCT circular scan and its vessels are described in Figure 1(I). The EM algorithm took 11 iterations to estimate the location of the scan circle in this example. Relative rotation of this scan circle w.r.t. the fundus image was 3.5° and was corrected when plotting the OCT vessels in Figure 4(I). The algorithm was successful in aligning the vessels in the images and this is quantified by the MAAD between the matched vessels having a relatively small value of 0.4°. In this example, most OCT vessels (from a to i) could be aligned to the fundus image vessels, as indicated by the large posterior probabilities $P(\mathbf{Y}_{i1} = 1 \mid \mathbf{X}_i)$ which are also given in Figure 4(I). On the other hand, one OCT vessel (x) could not be aligned to any fundus image vessel because in this case $P(\mathbf{Y}_{i1} = 1 \mid \mathbf{X}_i)$=0. The OCT image in Figure 1(II) shows that the detection of this 'vessel' may be a false positive result by the OCT vessel

detection algorithm because it isn't clear from looking at the image alone that there should be a vessel at that location. The vessel matching was decided by the largest posterior probabilities among $P\left(\mathbf{Z}_{ij'}|\mathbf{X}_i\right)$ for $j'=1$ to M which were denoted in Figure 4(I).

The algorithm produced successful inference of scan circle displacement for all OCT images. On average, the mean and SD of MAAD for all OCT circular scans (n=1242) in this sample of eyes were $0.82^{\circ}\pm0.34^{\circ}$. The average number of detected vessels in these OCT images was 11.6. On average, 86% of the OCT vessels could be aligned to fundus images with posterior probabilities $P\left(\mathbf{Y}_{i1}=1|\mathbf{X}_i\right)>P\left(\mathbf{Y}_{i0}=1|\mathbf{X}_i\right)$. Therefore, the average number of matched vessels is 10 (11.6×86%), suggesting that, although 14% of the vessels were not matched, the algorithm could terminate with successful inference (criteria described in Section IID) 'agreed' by the majority of the vessels and was able to align the OCT vessels to the fundus image vessels with minimal angular difference.

Locations of the 69 repeated circular scans from the same example eye are shown in Figure 4(II). Although the operator aimed to scan the same circular area on the retina, the scan circles, as inferred by the algorithm, are displaced from each other and covered a wide annulus area around the ONH. The distance (relative shift in microns and as degrees of relative rotation) between the centre of each scan circle, as determined by the algorithm, was calculated for all possible pairs of scans (n=2346). In the example shown in Figure 4, the mean distance between two scan circles was 143um (SD of 130µm) and relative rotation was 1.9º (SD of 1.8º).
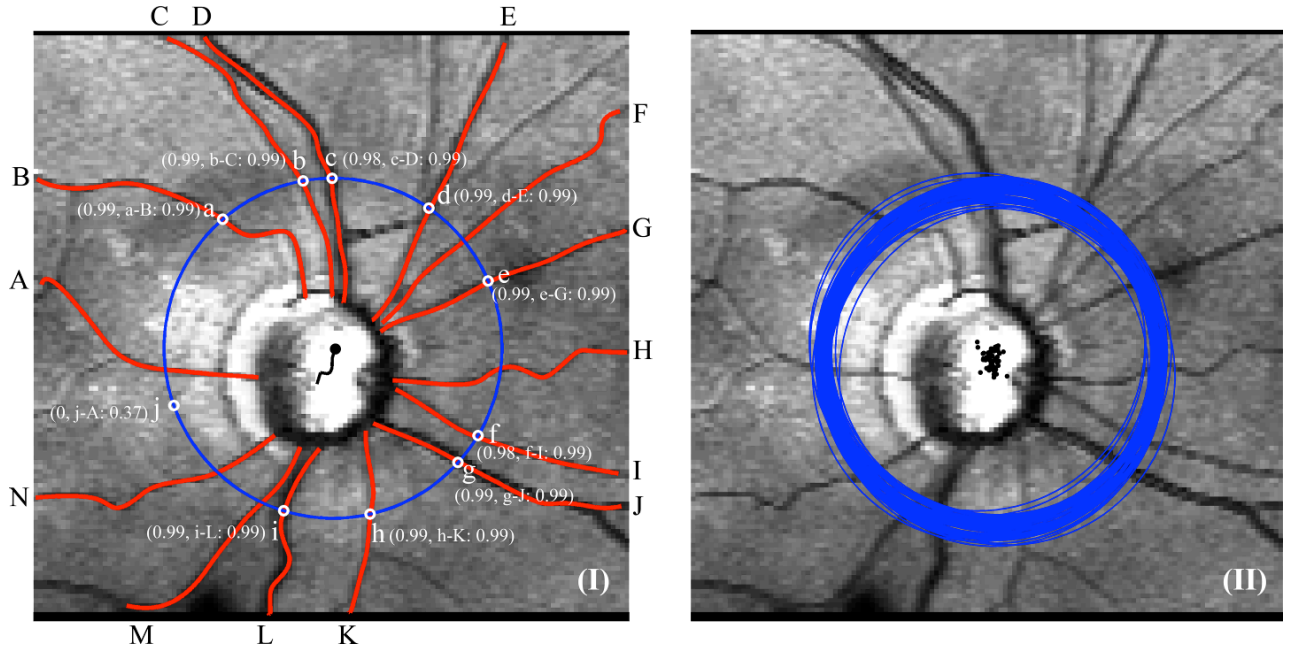

Figure 4. An example of OCT scan circle alignment algorithm. The initial location of the OCT scan circle and its vessels were described in Figure 1(I) and the initial rotation was 0°. The OCT scan circle and its vessels were superimposed on the fundus image (I) at the inferred location (black dot) and rotation (3.5°). The path of the scan circle centre at each step of the EM algorithm was plotted as a black curve on the fundus image. The posterior probability $P(\mathbf{Y}_{i1}=1|\mathbf{X}_i)$ and $P(\mathbf{Z}_{ij}|\mathbf{X}_i)$ for the matched fundus image vessel is denoted in the bracket beside each OCT vessel in the format of $(P(\mathbf{Y}_{i1}=1|\mathbf{X}_i)$, matched vessel pair: $P(\mathbf{Z}_{ij}|\mathbf{X}_i))$.

TABLE 1. DISTANCES AND ROTATION DIFFERENCE (MEAN±SD) BETWEEN TWO CIRCULAR SCANS

	All scans	Three consecutive scans
Distance on x-axis	88±91µm	29±36µm
Distance on y-axis	117±103µm	34±43µm
Overall distance	153±122µm	49±77µm
Rotation difference	1.7°±1.8°	0.8°±1.6°

During the OCT image acquisition, 3 scans are taken consecutively within 1.92 second after the manual placement of scan circle so the locations of the scan 'triplet' are expected to be affected less by the circle placement. To examine the assumption, the distances on the x-axis, y-axis, the overall distances in microns and the rotational distances in degree between all pairs of scan circles were calculated for each eye.

These distances were compared with those calculated with scan circle pairs from three consecutive scans during the same image acquisition. The mean and SD of these distances were summarized in TABLE 1, showing that, on average, the distance between two circular scans tends to be smaller if they belong to the scan triplet from the same image acquisition.

B. Effect of scan circle displacement on RNFLT

The impact of scan circle displacement on RNFLT measurement was examined. Quadrant RNFLT measurements (temporal, superior, nasal and inferior) were plotted against x-axis and y-axis displacements of the centre of each scan circle. Linear regression then gave estimates of the average change of quadrant RNFLT caused by the displacement of scan circle. An example from one eye is shown in Figure 5.

The superior and nasal RNFLT are negatively correlated with the scan circle location on y- and x-axis respectively. Similarly the inferior and temporal RNFLT are positively correlated with the scan circle location on y- and x-axis respectively. On average, the inferior RNFLT increases by $3.9 \pm 0.4 \mu m$ and the superior RNFLT decreases by $4.2 \pm 0.4 \mu m$ when the y-coordinate of scan circle centre increases by $100 \mu m$; the temporal RNFLT increases by $3.5 \pm 0.4 \mu m$ and the nasal RNFLT decreases by $4.2 \pm 0.5 \mu m$ when the x-coordinate of scan circle centre increases by $100 \mu m$.
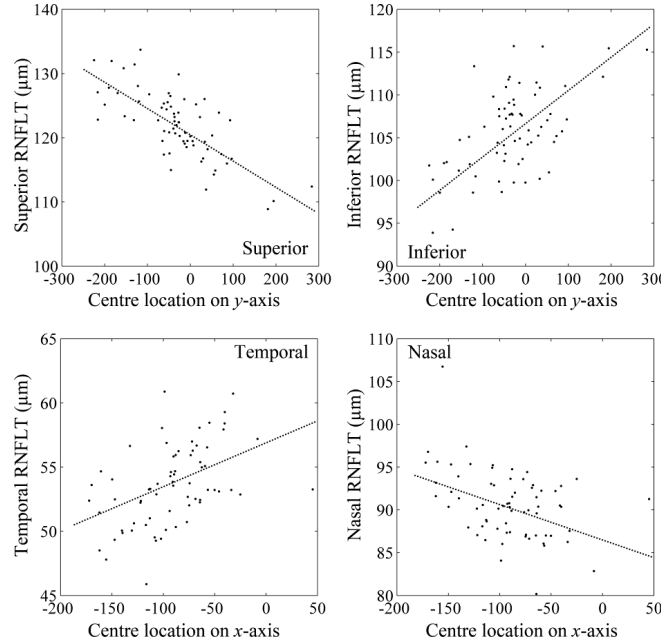

Figure 5. Plot of quadrant RNFLT measurements against the scan circle centre locations on x- and y-axis from one eye with fitted linear regression lines. The origin point (0μm) of the scan circle centre was arbitrarily chosen within the ONH. The slopes of the lines all differ from 0 (p<0.01).

The impact of scan circle displacement on RNFLT can also be observed by the change of RNFLT profile under scan circles at different locations. Figure 6 shows four scan circles relatively displaced towards superior, inferior, temporal and nasal directions. Note that the RNFLT profiles feature a 'double hump' shape where the RNFLT in superior and inferior areas is thicker than that in temporal and nasal regions. It is clear that moving the scan circle inferiorly increases the superior RNFLT and decreases the inferior RNFLT, and vice versa. Similarly, the scan circle on the nasal side has relatively thicker temporal RNFLT and thinner nasal RNFLT compared with the scan circle on the temporal side.
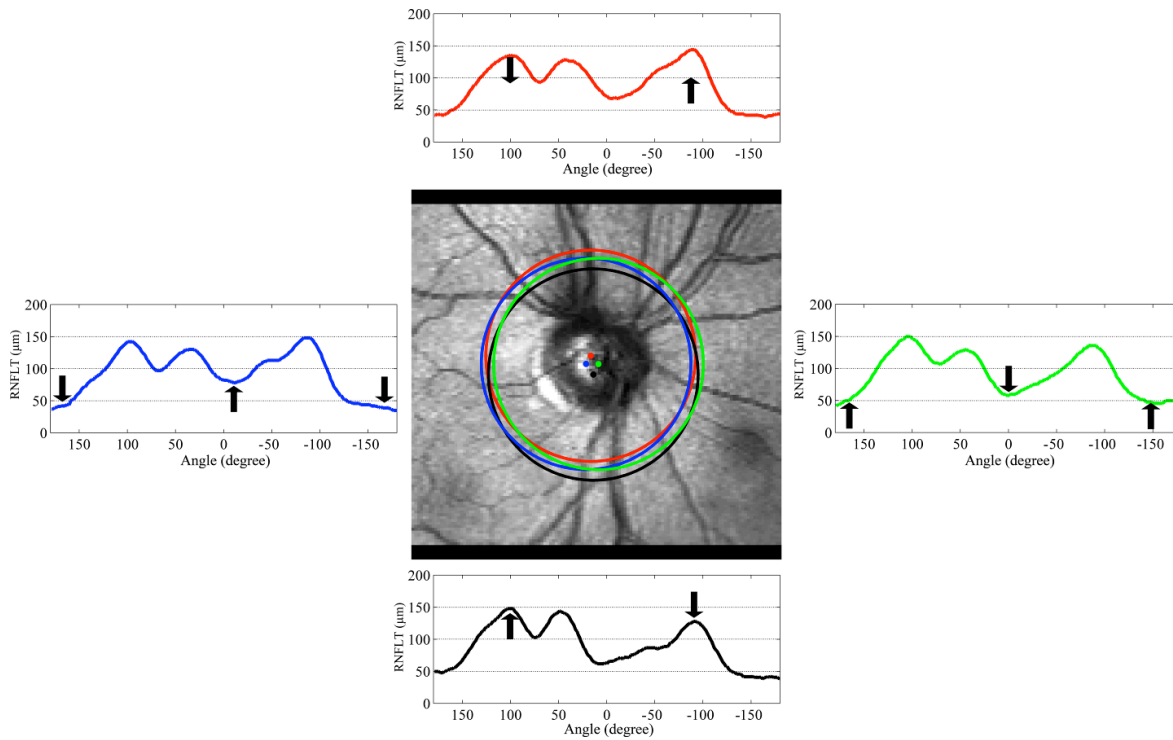
Figure 6. The RNFLT profile under scan circles at different locations on the retina. The scan circles at different locations were superimposed on the fundus image. These four scan circles were relatively superior (red), inferior (black), temporal (blue) and nasal (green) to each other. The tendency of change on RNFLT profile caused by the displacement of the scan circle location is indicated by the arrows in RNFLT profile plots. In each RNFLT profile plot, the *x*-axis is the peripapillary angle in the OCT circular scan.

C. RNFLT measurement variability

The RNFLT change caused by the scan circle displacement contributes to the variability of RNFLT measurement. The effect of scan circle displacement on mean and quadrant RNFLT measurement variability was investigated. Variability was scored as two times the standard deviation of three repeated scans [35], which were drawn from the exhaustive combination of all repeated scans of each eye. The average variability was calculated with all repeated scans and those scans with average distance among scan circle centres smaller than 50µm and larger than 300µm (Table 2). In short, the former represent a group of circular scans that the technique revealed to be closely matched, while the latter are scans that are more disparate.

RNFLT measurements (both mean and quadrant RNFLT) under the scan circles that are close to each other (average distance <50µm) demonstrates significantly lower (paired t-test; p<0.001) variability compared with those measured under scan circles that are far away from each other (average distance >300µm). This shows that the variability of RNFLT measurement is affected by the scan circle displacement and the scan circles that are close to each other provide RNFLT measurements with significantly better reproducibility.

TABLE 2. MEAN AND QUADRANT RNFLT VARIABILITY WITH ALL REPEATED SCANS AND SCANS WITH DIFFERENT AVERAGE DISTANCES AMONG SCAN CIRCLE CENTRES

	<50µm	>300µm	All scans
Mean RNFLT	4.3	7.4	6.2
Temporal RNFLT (µm)	6.8	10.7	8.9
Superior RNFLT (µm)	8.5	14.9	12.7
Nasal RNFLT (µm)	9.7	15.1	13.9
Inferior RNFLT (µm)	8.3	14.7	11.2

IV. DISCUSSION

Retinal vessels, compared with other RNFL structures, are relatively stable features for tracking a patient with glaucoma over time. This makes it possible to align multiple OCT circular scans, acquired in time, to a uniform coordinate formed by the vessel structures in the retinal fundus image. The two tasks in scan circle alignment, vessel matching and scan circle displacement inference, however, interact in a complicated way and have not been studied previously. The scan circle alignment algorithm proposed in this study integrated these two interactive steps into an EM framework: the iterative E- and M-steps in the algorithm incorporate the vessel matching, parameter inference and their interaction in a natural way. The algorithm guarantees to find a local maximum that gives an optimal alignment between two types of images.

Despite the superior specifications of the new SD-OCT, recent studies found that the diagnostic capability of TD-OCT is no worse than that of SD-OCT in clinical management of glaucoma [36-38] and other retinal diseases [39]. Particularly, the reproducibility for TD-OCT, for 'closely-matched' scans (average distance among scan circles <50µm in Table 2) identified by the algorithm, is close to reported reproducibility for SD-OCT [40, 41]. Therefore, many glaucoma services

'inheriting' TD-OCT from their retina specialist colleagues as they migrate to SD-OCT, may be confident that the TD-OCT provides similar monitoring capabilities for glaucoma as current SD-OCT devices.

The rate of RNFLT change caused by scan circle displacement demonstrated in Section IIIB (3.5μm in temporal, 4.2μm in superior, 4.2μm in nasal and 3.9μm in inferior when scan circle displaces by 100μm on *x*- and *y*-axis) is significant when compared with the variability of RNFLT measurement in Table 2. Dividing the rate of RNFLT change by the RNFLT variability with all scan circles in Table 2 shows that, on average, 39%, 33%, 30%, 35% of the variability in the temporal, superior, nasal and inferior quadrants can be explained by the scan circle displacement of 100μm, which is a significant amount of displacement compared with the average displacement in TABLE 1 (88μm on *x*-axis, 117μm on *y*-axis and overall 153μm).

The results from the validation experiment indicate that the variable location of the scan circle adversely affects the reproducibility of RNFLT measurements. RNFLT measurements and estimates of the corresponding displacement of the scan circles used together would be clinically useful when following a patient over time. The alignment algorithm, when applied retrospectively to data, will identify measurements that might be expected to have high variability. The technique, therefore, could provide a quality measure of scan acquisition, and this could even be achieved at the point of image acquisition. Moreover, the scan circle alignment algorithm can be used to identify those RNFLT measurements from areas that are close to each other. For multiple scans acquired at different periods of time, the RNFLT measurements that are identified as more reproducible may better reveal the real physiological change of the RNFLT in the longitudinal assessment of glaucoma. This will, therefore, have clinical impact on monitoring the progression of glaucoma over time. A recent study about the rate of RNFLT change caused by glaucoma reported decrease rates between −1.2μm/year and −15.4μm/year of mean RNFLT over a 5-year period [42]. We have shown that the scan circle alignment yields about a 30% reduction in the variability associated with average RNFLT measurements (Table 2: 6.2μm to 4.3μm). This better reproducibility (lower variability) of the RNFLT measurement means that fewer scans would be needed to detect the 'progression signal', potentially saving patient visits and resources. Moreover, the better reproducibility allows for earlier identification of progression and more accurate determination of a progression rate in a shorter period of time, which leads to more appropriate treatment, targeting more aggressive treatment of fast progressors and not over-treating those falsely believed to progressing rapidly because of noisy data.

The algorithm proposed in this study also helps to bridge OCT to the other imaging techniques such as SLP so the power of these techniques can be improved by their combination. It was shown, in a recent study [19], that the reproducibility of the calculated RNFL birefringence was improved when the OCT scan circle is aligned to the SLP image using the alignment algorithm.
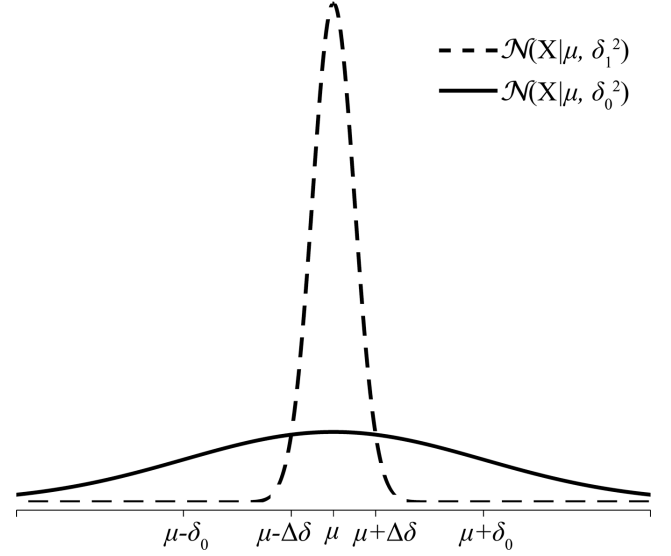

Figure 7. Illustration of the mixture of Gaussian distributions in Equation (6) for vessel matching. The two Gaussian distributions centre on the same mean $\mu = f_j(s, t, \theta)$ but have different standard deviations satisfying $\delta_1 \ll \delta_0$. The two Gaussian distributions intercept at two points that are $\Delta\delta$ from μ.

The vessel matching in the scan circle alignment algorithm is 'encoded' by two unobserved variables $\mathbf{Y}_i$ and $\mathbf{Z}_i$. The mixture of Gaussian distributions conditioned on $\mathbf{Y}_i$ in Equation (6) indicates whether the OCT vessel $\mathbf{X}_i$ can be aligned to a fundus image vessel and plays a key role in the algorithm. Figure 7 illustrates the mixture of Gaussian distributions with the same mean centred on a fundus image vessel but with different standard deviations $\delta_1 \ll \delta_0$. An OCT vessel follows a peaked distribution around the fundus image vessel and scores a high probability if these two vessels are close enough. The 'closeness' is defined by the two interceptions of two Gaussian distributions that are $\Delta\delta$ away from the mean. On the other hand, if the distance between the two vessels is not close enough (beyond the two interceptions), the probability of the Gaussian defined by δ_1 drops under the Gaussian defined by δ_0. In this case, the OCT vessel is 'forced' to follow the more 'uniform' distribution in order to score a relatively higher probability.

OCT vessels that cannot be aligned to any fundus image vessel (named here as 'noisy' vessels such as OCT vessel 'j' in Figure 4(I)) considerably mislead the parameter inference because their large distances from fundus image vessels dramatically affect the maximisation of the third term in Equation (13). The usage of the Gaussian mixture model helps to isolate the effect of these 'noisy' vessels. As an illustration, these 'noisy' vessels are all forced to follow a more uniform distribution (Figure 7) and thus have low probability values (defined in Equation (6)) near to zero. This, in turn, results in small $\boldsymbol{\alpha}_{ij}$ and $\boldsymbol{\beta}_{ij}^k$ for the corresponding 'noisy' vessels in the E-step. These near-to-zero values, once substituted into the objective function Equation (13) in the M-step, have minimal

effect on the objective function as well as its derivatives with respect to the scan circle displacement parameters. This process ensures that the 'noisy' vessels do not interfere with the parameter inference.

Instead of using fixed values for the standard deviation δ_1 and δ_0, the model was adjusted to infer (data not shown) δ_1 and δ_0 from the data in the EM algorithm. However, the inference algorithm tended to increase δ_1 and decrease δ_0 so that more OCT vessels are matched to the fundus image vessel even with a large angular difference. This approach increased the likelihood in Equation (9) because more OCT vessels follow the 'peaked' Gaussian distribution in the Gaussian mixture even if they are not well aligned, but the accuracy of the alignment is worse (larger MAAD) at the same time due to the larger δ_1 (Figure 3). Therefore, δ_1 and δ_0 are fixed as described in Section IIE. The chosen standard deviation of $\delta_1 = 2^o$ is small enough to meet the requirement of alignment accuracy and can incorporate the possible variance of vessel locations caused by factors such as potential eye movement during the image acquisition and possible physiological vessel shift over a long period of time. If the interceptions between the two Gaussian distributions are defined to be at $\Delta\delta = 2.5\delta_1$ away from the mean, the δ_0 is calculated to be 45°.

Last but not least, as illustrated in Figure 4, if a large sample of repeated circular scans were acquired, then they might cover an annulus area around the ONH potentially allowing for a three-dimensional RNFLT profiles to be reconstructed. We have previously shown that this might be a way of bridging measurements acquired with StratusOCT and those volume measurements from more recently established SD-OCT systems [43].

References

[1] D. Huang, E. A. Swanson, C. P. Lin, J. S. Schuman, W. G. Stinson, W. Chang, M. R. Hee, T. Flotte, K. Gregory, C. A. Puliafito, and J. G. Fujimoto, "Optical coherence tomography," *Science,* vol. 254, pp. 1178-1181, 1991.

[2] M. E. v. Velthoven, D. J. Faber, F. D. Verbraak, T. G. v. Leeuwen, and M. D. d. Smet, "Recent developments in optical coherence tomography for imaging the retina," *Prog. Retin. Eye Res.,* vol. 6, pp. 57-77, 2007.

[3] J. S. Schuman, M. R. Hee, A. V. Arya, T. Pedut-Kloizman, C. APuliafito, J. G. Fujimoto, and E. A. Swanson, "Optical coherence tomography: a new tool for glaucoma diagnosis," *Curr Opin Ophthalmol,* vol. 6, pp. 89-95, 2005.

[4] M. R. Hee, J. A. Izatt, E. A. Swanson, D. Huang, J. S. Schuman, C. P. Lin, C. A. Puliafito, and J. G. Fujimoto, "Optical coherence tomography of the human retina.," *Arch Ophthalmol,* vol. 113, pp. 325-332, 1995.

[5] P. Carpineto, M. Ciancaglini, E. Zuppardi, G. Falconio, E. Doronzo, and L. Mastropasqua, "Reliability of nerve fiber layer thickness measurements using optical coherence tomography in normal and glaucomatous eyes," *Ophthalmology,* vol. 110, pp. 190-195, 2003.

[6] R. R. Bourne, F. A. Medeiros, C. Bowd, K. Jahanbakhsh, L. M. Zangwill, and R. N. Weinreb, "Comparability of Retinal Nerve Fiber Layer Thickness Measurements of Optical Coherence Tomography Instruments," *Invest Ophthalmol Vis Sci,* vol. 46, pp. 1280-1285, 2005.

[7] J. S. Schuman, T. Pedut-Kloizman, H. Pakter, N. Wang, V. Guedes, L. Huang, L. Pieroth, W. Scott, M. R. Hee, J. G. Fujimoto, H. Ishikawa, R. A. Bilonick, L. Kagemann, and G. Wollstein, "Optical Coherence Tomography and Histologic Measurements of Nerve Fiber Layer Thickness in Normal and Glaucomatous Monkey Eyes," *Invest Ophthalmol Vis Sci,* vol. 48, pp. 3645-3654, 2007.

[8] M. L. Gabriele, H. Ishikawa, G. Wollstein, R. A. Bilonick, K. A. Townsend, L. Kagemann, M. Wojtkowski, V. J. Srinivasan, J. G. Fujimoto, J. S. Duker, and J. S. Schuman, "Optical coherence tomography scan circle location and mean retinal nerve fiber layer measurement variability," *Invest Ophthalmol Vis Sci,* vol. 49, pp. 2315-2321, 2008.

[9] G. Vizzeri, C. Bowd, F. A. Medeiros, R. N. Weinreb, and L. M. Zangwill, "Effect of improper scan alignment on retinal nerve fiber layer thickness measurements using Stratus optical coherence tomograph," *J Glaucoma,* vol. 17, pp. 341-349, 2008.

[10] G. Vizzeri, C. Bowd, F. A. Medeiros, R. N. Weinreb, and L. M. Zangwill, "Effect of signal strength and improper alignment on the variability of stratus optical coherence tomography retinal nerve fiber layer thickness measurements," *Am J Ophthalmol,* vol. 148, pp. 249-255 e1, 2009.

[11] M. Bock, A. U. Brandt, J. Dorr, C. F. Pfueller, S. Ohlraun, F. Zipp, and F. Paul, "Time domain and spectral domain optical coherence tomography in multiple sclerosis: a comparative cross-sectional study," *Mult Scler,* vol. 16, pp. 893-6, 2010.

[12] A. F. Fercher, C. K. Hitzenberger, G. Kamp, and S. Y. El-Zaiat, "Measurement of intraocular distances by backscattering spectral interferometry," *Opt Commun,* vol. 117, pp. 43-48, 1995.

[13] M. Wojtkowski, R. Leitgeb, A. Kowalczyk, T. Bajraszewski, and A. F. Fercher, "In vivo human retinal imaging by Fourier domain optical coherence tomography," *J Biomed Opt,* vol. 7, pp. 457-463, 2002.

[14] N. Nassif, B. Cense, B. H. Park, S. H. Yun, T. C. Chen, B. E. Bouma, G. J. Tearney, and J. F. d. Boer, "In vivo human retinal imaging by ultrahigh-speed spectral domain optical coherence tomography," *Opt Lett,* vol. 29, pp. 480-482, 2004.

[15] R. Leitgeb, C. K. Hitzenberger, and A. F. Fercher, "Performance of fourier domain vs. time domain optical coherence tomography," *Opt Express,* vol. 11, pp. 889-894, 2003.

[16] J. F. d. Boer, B. Cense, B. H. Park, M. C. Pierce, G. J. Tearney, and B. E. Bouma, "Improved signal-to-noise ratio in spectral-domain compared with time-domain optical coherence tomography," *Opt Lett,* vol. 28, pp. 2067-2069, 2003.

[17] G. Vizzeri, R. N. Weinreb, A. O. Gonzalez-Garcia, C. Bowd, F. A. Medeiros, P. A. Sample, and L. M. Zangwill, "Agreement between spectral-domain and time-domain OCT for measuring RNFL thickness," *British Journal of Ophthalmology,* vol. 93, pp. 775-781, 2009.

[18] J. S. Kim, H. Ishikawa, M. L. Gabriele, G. Wollstein, R. A. Bilonick, L. Kagemann, J. G. Fujimoto, and J. S. Schuman, "Retinal Nerve Fiber Layer Thickness Measurement Comparability between Time Domain Optical Coherence Tomography (OCT) and Spectral Domain OCT," *Invest Ophthalmol Vis Sci,* vol. 51, pp. 896-902, 2010.

[19] M. Sehi, D. S. Grewal, H. Zhu, W. J. Feuer, and D. S. Greenfield, "Quantification of change in axonal birefringence following surgical reduction in IOP," *Ophthalmic Surg Lasers Imaging,* Accepted, In Press. 2010.

[20] J. V. B. Soares, J. J. G. Leandro, R. M. Cesar, H. F. Jelinek, and M. J. Cree, "Retinal vessel segmentation using the 2-D Gabor wavelet and supervised classification," *Medical Imaging, IEEE Transactions on,* vol. 25, pp. 1214-1222, 2006.

[21] J. Staal, M. D. Abramoff, M. Niemeijer, M. A. Viergever, and B. van Ginneken, "Ridge-based vessel segmentation in color images of the retina," *Medical Imaging, IEEE Transactions on,* vol. 23, pp. 501-509, 2004.

[22] F. Zana and J. C. Klein, "Segmentation of vessel-like patterns using mathematical morphology and curvature evaluation," *Image Processing, IEEE Transactions on,* vol. 10, pp. 1010-1019, 2001.

[23] A. D. Hoover, V. Kouznetsova, and M. Goldbaum, "Locating blood vessels in retinal images by piecewise threshold probing of a matched filter response," *Medical Imaging, IEEE Transactions on,* vol. 19, pp. 203-210, 2000.

[24] J. Xiaoyi and D. Mojon, "Adaptive local thresholding by verification-based multithreshold probing with application to vessel detection in retinal images," *Pattern Analysis and Machine Intelligence, IEEE Transactions on,* vol. 25, pp. 131-137, 2003.

[25] B. S. Y. Lam, G. Yongsheng, and A. W. C. Liew, "General Retinal Vessel Segmentation Using Regularization-Based Multiconcavity Modeling," *Medical Imaging, IEEE Transactions on,* vol. 29, pp. 1369-1381, 2010.

[26] A. F. Frangi, W. J. Niessen, K. L. Vincken, and M. A. Viergever, "Multiscale vessel enhancement filtering," *Medical Image Computing and Computer-Assisted Intervention* pp. 130-137, 1998.

[27] J. H. Ahlberg, E. N. Nilson, and J. L. Walsh, "The theory of splines and their applications," vol. 38, ed. New York: Academic Press, 1967.

[28] M. D. Zio, U. Guarnera, and R. Rocci, "A mixture of mixture models for a classification problem: The unity measure error," *Computational Statistics & Data Analysis,* vol. 51, pp. 2573-2585, 2007.

[29] J. Qin and D. H. Leung, "A semiparametric two-component "compound" mixture model and its application to estimating malaria attributable fractions," *Biometrics,* vol. 61, pp. 456-64, 2005.

[30] A. P. Dempster, N. M. Laird, and D. B. Rubin, "Maximum likelihood from incomplete data via the EM algorithm," *Journal of the Royal Statistical Society: Series B,* vol. 39, pp. 1-38, 1977.

[31] E. Polak, *Computational methods in optimization: a unified approach*. New York: Academic Press, 1971.

[32] R. Fletcher, *Practical methods of optimization (2nd ed.)*. New York: John Wiley & Sons, 1987.

[33] C. M. Bishop, *Neural network for pattern recognition*: Oxford University Press, 1996.

[34] G. Wollstein, J. S. Schuman, L. L. Price, A. Aydin, P. C. Stark, E. Hertzmark, E. Lai, H. Ishikawa, C. Mattox, J. G. Fujimoto, and L. A. Paunescu, "Optical coherence tomography longitudinal evaluation of retinal nerve fiber layer thickness in glaucoma," *Arch Ophthalmol,* vol. 123, pp. 464-70, 2005.

[35] D. L. Budenz, R. T. Chang, X. Huang, R. W. Knighton, and J. M. Tielsch, "Reproducibility of Retinal Nerve Fiber Thickness Measurements Using the Stratus OCT in Normal and Glaucomatous Eyes," *Invest Ophthalmol Vis Sci,* vol. 46, pp. 2440-2443, 2004.

[36] C. K. Leung, C. Y. Cheung, R. N. Weinreb, Q. Qiu, S. Liu, H. Li, G. Xu, N. Fan, L. Huang, C. P. Pang, and D. S. Lam, "Retinal nerve fiber layer imaging with spectral-domain optical coherence tomography: a variability and diagnostic performance study," *Ophthalmology,* vol. 116, pp. 1257-1263.e2, 2009.

[37] J. W. Cho, K. R. Sung, J. T. Hong, T. W. Um, S. Y. Kang, and M. S. Kook, "Detection of Glaucoma by Spectral Domain-scanning Laser Ophthalmoscopy/Optical Coherence Tomography (SD-SLO/OCT) and Time Domain Optical Coherence Tomography," *J Glaucoma,* vol. Publish Ahead of Print, p. 10.1097/IJG.0b013e3181d1d332, Apr 29 2010.

[38] M. Sehi, D. S. Grewal, C. W. Sheets, and D. S. Greenfield, "Diagnostic ability of Fourier-domain vs time-domain optical coherence tomography for glaucoma detection," *Am J Ophthalmol,* vol. 148, pp. 597-605, Oct 2009.

[39] F. Forooghian, C. Cukras, C. B. Meyerle, E. Y. Chew, and W. T. Wong, "Evaluation of Time Domain and Spectral Domain Optical Coherence Tomography in the Measurement of Diabetic Macular Edema," *Invest Ophthalmol Vis Sci,* vol. 49, pp. 4290-4296, 2008.

[40] J. S. Kim, H. Ishikawa, K. R. Sung, J. Xu, G. Wollstein, R. A. Bilonick, M. L. Gabriele, L. Kagemann, J. S. Duker, J. G. Fujimoto, and J. S. Schuman, "Retinal nerve fibre layer thickness measurement reproducibility improved with spectral domain optical coherence tomography," *Br J Ophthalmol,* vol. 93, pp. 1057-1063, 2009.

[41] J. C. Mwanza, R. T. Chang, D. L. Budenz, M. K. Durbin, M. G. Gendy, W. Shi, and W. J. Feuer, "Reproducibility of Peripapillary Retinal Nerve Fiber Layer Thickness and Optic Nerve Head Parameters Measured with CirrusTM HD-OCT in Glaucomatous Eyes," *Invest. Ophthalmol. Vis. Sci.,* p. Publish Ahead of Print, June 23, 2010 2010.

[42] C. K.-s. Leung, C. Y. L. Cheung, R. N. Weinreb, K. Qiu, S. Liu, H. Li, G. Xu, N. Fan, C. P. Pang, K. K. Tse, and D. S. C. Lam, "Evaluation of Retinal Nerve Fiber Layer Progression in Glaucoma: A Study on Optical Coherence Tomography Guided Progression Analysis," *Investigative Ophthalmology & Visual Science,* vol. 51, pp. 217-222, 2010.

[43] H. Zhu, D. P. Crabb, P. G. Schlottmann, and D. F. Garway-Heath, "Aligning Sequential Stratus OCT RNFL Scans - Solving the Problem," *Invest Ophthalmol Vis Sci,* vol. 48, pp. ARVO E-Abstract 516, 2007.